



Efficient Simulation of RC Shear Walls in High-Rise Buildings Using a Practical Multi-Cross-Line-Model

Baoyin Sun, Quan Gu, Peizhou Zhang, Yong Li & Jinping Ou

To cite this article: Baoyin Sun, Quan Gu, Peizhou Zhang, Yong Li & Jinping Ou (2019): Efficient Simulation of RC Shear Walls in High-Rise Buildings Using a Practical Multi-Cross-Line-Model, Journal of Earthquake Engineering

To link to this article: <https://doi.org/10.1080/13632469.2019.1597785>



Published online: 08 Apr 2019.



Submit your article to this journal



View Crossmark data



Efficient Simulation of RC Shear Walls in High-Rise Buildings Using a Practical Multi-Cross-Line-Model

Baoyin Sun ^{a,b}, Quan Gu  ^{b,c}, Peizhou Zhang^a, Yong Li  ^d, and Jinping Ou^a

^aFaculty of Infrastructure Engineering, Dalian University of Technology, Dalian, China; ^bDepartment of Civil and Environmental Engineering, University of California, Berkeley, CA, USA; ^cSchool of Architecture and Civil Engineering, Xiamen University, Xiamen, China; ^dDepartment of Civil and Environmental Engineering, University of Alberta, Edmonton, Canada

ABSTRACT

This paper presents a novel model for reinforced concrete (RC) shear walls, named as multi-cross line model (MCLM), combining the concepts of micro- and macro-shear wall models by simulating the stress-strain relationships at the material level using a set of concrete or steel bars, and thereof calculating the resultant stresses. The two-dimensional MCLM jointly with the multilayer shell element can simulate the three-dimensional behaviors of the RC shear walls. The proposed model is validated by using three RC shear wall specimens under cyclic loading conditions. Besides, the huge potential for practical use of this model is also illustrated.

ARTICLE HISTORY

Received 6 October 2018
Accepted 17 March 2019

KEYWORDS

RC shear wall; nonlinear finite element model; multi-cross-line model; shear-flexure; nonlinear behavior

1. Introduction

Finite element modeling has been recognized as an analytical tool in the design and analysis of engineering structures, including reinforced concrete (RC) shear walls as the primary lateral force-resisting systems of high-rise buildings subject to horizontal wind or earthquake loads. In the past decades, there has been an urgent need for practical modeling strategies to simulate accurately and efficiently the nonlinear behaviors of the RC shear walls under cyclic loads. For this purpose, significant efforts have been taken to develop various models in research literatures. These models typically falls into two categories, namely, (1) micro-models mainly developed to achieve better understanding of the underlying physics with acceptable accuracy and (2) macro-models to capture the overall behavior of the structural system for efficiency. The micro-models study the constitutive behaviors of the RC shear walls at the material level (e.g., at a Gauss point of a finite element), while representing the cracked concrete by using continuous smeared-crack models. In contrast, the macro-models study the mechanical behaviors of RC shear walls using a set of discrete elements, e.g., trusses, frames, and springs. Before proposing the new shear wall model for a balance between the accuracy and efficiency in this study, this study conducts a brief literature review about existing micro-models and macro-models in the literature, respectively.

CONTACT Quan Gu  quangu@xmu.edu.cn  School of Architecture and Civil Engineering, Xiamen University, Xiamen 361005, China

Color versions of one or more of the figures in the article can be found online at www.tandfonline.com/ueqe.

© 2019 Taylor & Francis Group, LLC

Among various micro-models, the compression field theory (CFT) [Vecchio and Collins, 1981] and modified compression field theory (MCFT) [Vecchio and Collins, 1986] are widely used, in which the shear resistance is provided by concrete struts along the principal stress directions (i.e., the tangent and normal directions to cracks). The biaxial behavior of concrete is considered by incorporating the softening effect in the compressive strength, i.e., strength deterioration in the principal compressive direction due to the increasing tensile strain in the principal tensile direction. The MCFT has been further refined to the disturbed stress field model (DSFM) for RC structures by the same group of researchers at the University of Toronto in Canada. In the United States, Hsu and his coworkers developed another family of widely used micro-models, including the rotating-angle softened truss models (RA-STM) [Hsu, 1993; Belarbi and Hsu, 1995; Hsu *et al.*, 1995; Pang and Hsu, 1995], the fixed-angle softened truss model (FA-STM) [Hsu, 1996; Pang and Hsu, 1996], the softened membrane model (SMM) [Zhu, 2000; Hsu and Zhu, 2002], and the cyclic softened membrane model (CSMM) [Mansour, 2001; Mansour *et al.*, 2001; Mansour and Hsu, 2005a; Mansour and Hsu, 2005b; Hsu *et al.*, 2006]. These models assume that the direction of cracks is perpendicular to the direction of the principal tensile stress of concrete in RA-STM or the RC in FA-STM, SMM, and CSMM. In these models, the state-dependent Poisson's effect (i.e., relationship between the biaxial strains and uniaxial strains) is either ignored (e.g., in RA-STM and FA-STM) or studied elaborately using a time-varying Hsu/Zhu ratio (e.g., in SMM and CSMM).

In the second class of shear wall models, multiple macro-models exist in the literature with different features. To be specific, the three-vertical-line-element model (TVLEM) simulates the bending and shear behaviors of shear panels using three vertical line (truss) elements, one horizontal truss element, and one rotational spring element between two quasi-rigid beams at the top and bottom floor levels [Kabeyasawa *et al.*, 1983]. Similarly, the multi-vertical-line-element model (MVLEM) employs a set of vertical truss elements, and a horizontal spring element connecting with two rigid beams at the top and bottom floor levels [Vulcano and Bertero, 1987]. As a variant of TVLEM, the panel-wall macro element (PWME) modifies the TVLEM by replacing the horizontal and rotation truss elements with a plane element [Kabeyasawa, 1997]. The truss model (TM) proposed by Park and Eom discretizes the RC shear wall components into a set of horizontal, vertical, and diagonal truss elements, and the strength softening of the diagonal trusses is considered in the similar way as MCFT [Park and Eom, 2007]. Instead of using truss elements only, Panagiotou and his coworkers presented a cyclic beam-truss model (BTM) for non-planar RC walls. A set of nonlinear Euler–Bernoulli fiber-section beam elements are used to model the mechanical behaviors for the vertical direction and a set of nonlinear trusses for horizontal and diagonal directions (with the softening effect simulated similarly with the TM) [Panagiotou *et al.*, 2009, 2012; Lu and Panagiotou, 2014; Moharrami *et al.*, 2015]. The BTM is further developed and used in other studies about RC shear walls in the past few years [Barbosa, 2011].

With an appreciation of the existing shear wall models in the literature summarized above and others not mentioned, a novel two-dimensional (2D) model, termed as the multi-cross line model (MCLM), for shear walls is proposed by Sun *et al.* [2018]. The shear wall model aims at combining the concepts of micro- and macro-shear wall models by simulating the stress-strain relationships at the material level (e.g., at a Gauss point) using a set of concrete or steel bars, and thereof calculating the equivalent stresses. The

newly developed MCLM is implemented in the open-source general finite element (FE) software framework, *OpenSees* (abbreviated for Open System for Earthquake Engineering Simulation [McKenna, 1997; Fenves *et al.*, 2004; McKenna *et al.*, 2009]). Furthermore, a modified shell element is presented to model 3D shear walls, in which the in-plane nonlinear shearing behavior is simulated by using the MCLM while the out-plane force-deformation responses using linear elastic models.

The work of Sun *et al.* [2018] has been further enhanced mainly to improve the capacity of the MCLM model and to verify its numerical accuracy and computational efficiency. The new advancements of work compared with the previous conference paper are summarized below: (1) For MCLM, the sensitivities of the shear strength correction factor with respect to the parameters k_1 and k_2 are studied. (2) The tangent moduli of the MCLM is newly derived and implemented, which is important to guarantee the quadratic convergence of the NR iterative process for solving the non-linear system of equations of motion in the FE analysis. To emphasize such contribution, the rate of convergence is studied in detail. (3) Complicated 3D shear wall problems can be solved by combining the MCLM with multilayer shell element. For example, a tested T-shaped shear wall component from the literature is re-analyzed using the proposed MCLM model to validate its applicability for 3D RC shear walls. (4) Two representative planar shear wall specimens (different from previous work) and a 3D T-shaped shear wall component are studied with more insightful details. Many local responses (e.g., lateral displacement, concrete strain, steel strain.) are compared between predicted and experimental results. The discrepancies are quantified and well explained. The computational efficiency and numerical stability are studied. (5) The MCLM combined with multilayered shell element are used to perform the seismic analysis for a 32-story high-rise RC frame-shear wall building, to demonstrate the capacity of the model for large scale seismic analysis of tall buildings.

2. Formulation of the Multi-Cross-Line Model

To facilitate the development of MCLM, 2D membrane stress resultants are computed by combining stresses from two types of layers, i.e., a concrete layer and a reinforcing steel layer, based on the following assumptions summarized herein: (a) perfect bonding (i.e., no bond slip) between steel bars and surrounding concrete (see Fig. 1(a)); (b) the shear stress of the concrete layer is modeled by two diagonal concrete bars perpendicular to each other (Fig. 1(b)). Note that the compressive strength of each concrete bar softens (decreases) with the increase of the tensile strain of the other bar (normal to this bar). The horizontal and vertical normal stresses are attributed only to the two corresponding concrete bars; (c) the 2D stress of the steel layer is computed from the force of the rebar using a one-dimensional (1D) smeared steel material model. With these assumptions, the stress resultants for MCLM can be derived with the details described next.

The stress resultants at a material point of a RC shear wall include the horizontal, vertical, and shear stress components collected in the vector $[\sigma_l \sigma_t \tau_{lt}]^T$, as shown in Fig. 1(a). They are calculated from stresses of two layers (see Equation (1)), i.e., the stresses of the reinforcing steel layer ($[\sigma_l^s \sigma_t^s \tau_{lt}^s]^T$ shown in Fig. 1(b) and the stresses of the concrete layer ($[\sigma_l^c \sigma_t^c \tau_{lt}^c]^T$ shown in Fig. 1(c).

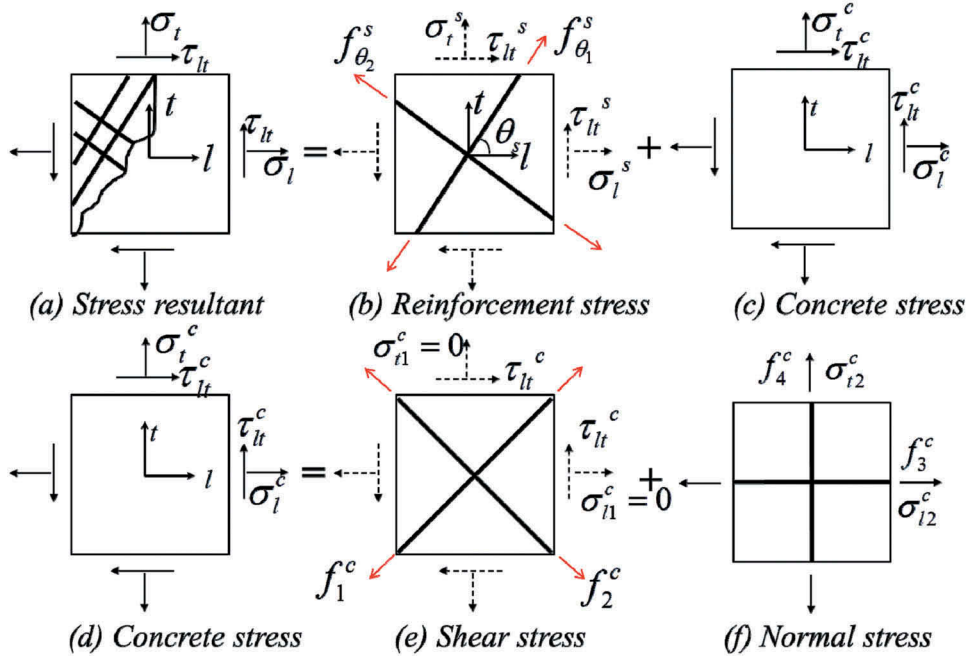


Figure 1. The multi-cross-line model.

$$\begin{Bmatrix} \sigma_l \\ \sigma_t \\ \tau_{lt} \end{Bmatrix} = \begin{Bmatrix} \sigma_l^s \\ \sigma_t^s \\ \tau_{lt}^s \end{Bmatrix} + \begin{Bmatrix} \sigma_l^c \\ \sigma_t^c \\ \tau_{lt}^c \end{Bmatrix} \quad (1)$$

For notational simplicity, the subscripts l and t denote the horizontal and vertical directions, respectively, and the superscripts s and c denote the steel and concrete material, respectively.

In Fig. 1(b), the stresses for the reinforcing steel layer are computed from uniformly distributed reinforcement assuming 1D smeared steel material model (i.e., $\rho_1 f_{\theta_1}^s$ and $\rho_2 f_{\theta_2}^s$, where ρ_i and $f_{\theta_i}^s$ denote the reinforcement ratio and stresses, respectively, with i indicating i th direction, $i = 1, 2$). Specifically, the stress in the steel can be derived from Equation (2).

$$\begin{Bmatrix} \sigma_l^s \\ \sigma_t^s \\ \tau_{lt}^s \end{Bmatrix} = \mathbf{T}(-\theta_1) \begin{Bmatrix} \rho_1 f_{\theta_1}^s \\ 0 \\ 0 \end{Bmatrix} + \mathbf{T}(-\theta_2) \begin{Bmatrix} \rho_2 f_{\theta_2}^s \\ 0 \\ 0 \end{Bmatrix} \quad (2)$$

where $\mathbf{T}(\theta_i)$ ($i = 1, 2$) is the coordinate transformation matrix, and θ_i ($i = 1, 2$) is the angle between the direction of the i th reinforcing steel and the horizontal direction (l -direction) with the counter-clockwise as positive. The matrix $\mathbf{T}(\theta_i)$ reads as,

$$\mathbf{T}(\theta_i) = \begin{bmatrix} \cos^2 \theta_i & \sin^2 \theta_i & 2 \sin \theta_i \cos \theta_i \\ \sin^2 \theta_i & \cos^2 \theta_i & -2 \sin \theta_i \cos \theta_i \\ -\sin \theta_i \cos \theta_i & \sin \theta_i \cos \theta_i & \cos^2 \theta_i - \sin^2 \theta_i \end{bmatrix} \quad (3)$$

A smeared uniaxial steel material model in Mansour *et al.* [2001] is adopted to compute the stress $f_{\theta_i}^s$ of the reinforcing bar depending on the strain along the i th direction (i.e., $\varepsilon_{\theta_i}^s$) obtained by transforming the strain at the Gauss point (i.e., $[\varepsilon_l \quad \varepsilon_t \quad \gamma_{lt}/2]^T$) following Equation (4),

$$\varepsilon_{\theta_i}^s = [1 \quad 0 \quad 0]^T \mathbf{T}(\theta_i) \{ \varepsilon_l \quad \varepsilon_t \quad \gamma_{lt}/2 \}^T \quad (4)$$

For the concrete layer, the total stress (see Fig. 1(d)) is computed from the pair of two diagonal bars (see Fig. 1(e)) and the other two (horizontal and vertical) bars (Fig. 1(f)), i.e.,

$$\begin{Bmatrix} \sigma_l^c \\ \sigma_t^c \\ \tau_{lt}^c \end{Bmatrix} = \begin{Bmatrix} \sigma_{l1}^c \\ \sigma_{t1}^c \\ \tau_{lt}^c \end{Bmatrix} + \begin{Bmatrix} \sigma_{l2}^c \\ \sigma_{t2}^c \\ 0 \end{Bmatrix} \quad (5)$$

The shear stress τ_{lt}^c (Fig. 1(e)) for the concrete layer is calculated using two cross diagonal bars, which are perpendicular to each other and having 45 degree with the horizontal direction. Since the stresses of the two diagonal bars (i.e., f_1^c and f_2^c) are assumed to have no contribution to the normal stress (i.e., σ_{l1}^c and σ_{t1}^c) based on assumption (b), the two diagonal bars contribute to the shear stress only, i.e., $\sigma_{l1}^c = \sigma_{t1}^c = 0$ in Fig. 1(e) and Equation (6).

$$\begin{Bmatrix} \sigma_{l1}^c \\ \sigma_{t1}^c \\ \tau_{lt}^c \end{Bmatrix} = \begin{Bmatrix} 0 \\ 0 \\ \tau_{lt}^c \end{Bmatrix} = \begin{bmatrix} 0 & 0 & 0 \\ 0 & 0 & 0 \\ 0 & 0 & \zeta \end{bmatrix} \mathbf{T}\left(-\frac{\pi}{4}\right) \begin{Bmatrix} f_1^c \\ f_2^c \\ 0 \end{Bmatrix} \quad (6)$$

where f_1^c and f_2^c denote the stresses of the two cross diagonal concrete bars (see Fig. 1(e)), respectively; parameter ζ is a shear strength correction factor to account for the area reduction and vertical compression effect, which will be explained in detail later. The normal stresses (i.e., σ_{l2}^c and σ_{t2}^c in Fig. 1(f)) are calculated using two uncoupled concrete bars (i.e., f_3^c and f_4^c in Fig. 1(f)) along the two normal directions, that is,

$$[\sigma_{l2}^c \quad \sigma_{t2}^c \quad 0]^T = [f_3^c \quad f_4^c \quad 0]^T \quad (7)$$

where f_3^c and f_4^c are stresses of the concrete bars along the horizontal and vertical directions (see Fig. 1(f)), respectively. To account for the compression softening, the compressive strength of one diagonal bar is reduced with the increasing tensile strain in the other concrete bar. The stress on the four concrete bars (i.e., $f_i^c (i = 1, 2, 3, 4)$) are computed based on the strains in the four directions, respectively. Given the strain state at a material point (i.e., $[\varepsilon_l \quad \varepsilon_t \quad \gamma_{lt}]^T$), the strains along the diagonal directions can be calculated as,

$$\begin{Bmatrix} \varepsilon_1^c \\ \varepsilon_2^c \\ \varepsilon_{12}^c \end{Bmatrix} = \begin{bmatrix} 1 & 0 & 0 \\ 0 & 1 & 0 \\ 0 & 0 & 0 \end{bmatrix} \mathbf{T}\left(\frac{\pi}{4}\right) \begin{Bmatrix} \varepsilon_l \\ \varepsilon_t \\ \gamma_{lt}/2 \end{Bmatrix} \quad (8)$$

Note that the shear stresses along the diagonal directions (i.e., on the diagonal bars) are ignored in this model and therefore the corresponding shear strains ε_{12}^c in Equation (8) are set to be zero. The diagonal stresses f_1^c and f_2^c are computed from the strains of the two diagonal concrete bars (i.e., ε_1^c and ε_2^c). On the other hand, the concrete strains along the normal directions are the same as the normal components of the strains at the Gauss point, that is,

$$\varepsilon_l^c = \varepsilon_l, \quad \varepsilon_t^c = \varepsilon_t \quad (9)$$

2.1. The Shear Strength Correction Factor

In this study, a shear strength correction factor ζ is proposed (in Equation 6) to account for the influence of the effective areas of the diagonal concrete bars and the vertical compressive strain on the shear strength. The correction factor ζ is defined as a function of the maximum historical vertical compressive strain (ε_{maxc}), i.e.,

$$\zeta = \begin{cases} k_1 & \varepsilon_{maxc} \geq 0 \\ k_1 \exp(-k_2 \varepsilon_{maxc}) \leq 1 & \varepsilon_{maxc} < 0 \end{cases} \quad (10)$$

where value k_1 is the correction representing the area reduction coefficient of the diagonal concrete bars, and the term $\exp(-k_2 \varepsilon_{maxc})$ considers the shear strength change due to the vertical compressive strain of the concrete. The sensitivity of the shear strength correction factor with respect to (w.r.t.) the parameters k_1 and k_2 is illustrated in Fig. 2. Since the MCLM combines the micro and macro models through simulating the stress-strain relationship by using macro concrete bars, the area reduction approach typically used in macro models is applied, i.e., employing an equivalent (reduced) section area of the diagonal concrete bar to resist shear forces. When the maximum historical vertical compressive strain increases, the shear strength correction factor increases as indicated in Fig. 2. This factor is not highly sensitive to the parameters k_1 and k_2 , which are respectively suggested to be 0.25 and 1,500 based on investigations on existing experimental results in this study.

2.2. A Modified Uniaxial Model for Concrete Bars

To model realistically the 1D nonlinear behavior of the concrete bar, a smeared concrete model is developed by adapting the existing model in Belarbi and Hsu [1994]. In Fig. 3, C_1 and C_2 denote the pre-peak and post-peak compressive stress-strain envelopes, respectively; T_1 and T_2 indicate the pre-cracking and post-cracking tensile stress-strain

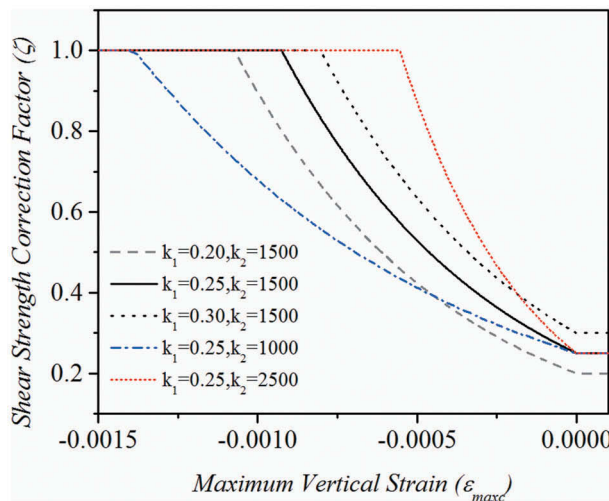


Figure 2. The sensitivity of the shear strength correction factor w.r.t. the parameters k_1 and k_2 .

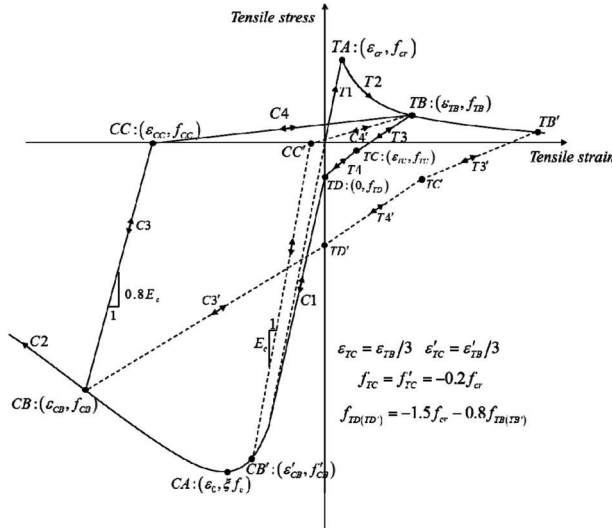


Figure 3. The smeared-crack concrete model.

envelopes, respectively. Parameters f_c and ϵ_0 are the compressive strength and the corresponding strain, and ξ is compressive strength reduction coefficient. Parameters f_{cr} and ϵ_{cr} represent the tensile strength and the corresponding cracking strain, respectively. The loading/unloading rules in the compression region are simplified, as shown in Fig. 3, in order to enhance the numerical stability of the MCLM. Post-peak unloading curve (i.e., the compressive stress-strain segment $C3$ in Fig. 3) at the point CB (ϵ_{CB}, f_{CB}) follows the straight line from reversed point CB to the point CC (ϵ_{CC}, f_{CC}). In such a case when the reversed point CB (ϵ_{CB}, f_{CB}) with strain ϵ_{CB} less than ϵ_0 (i.e., the absolute value of ϵ_{CB} is larger than that of ϵ_0), the tangent stiffness E_{CC} for this unloading segment is taken as $0.8E_c$ (i.e., 80% of the initial tangent stiffness). Otherwise, E_{CC} is taken as E_c , e.g., when unloading from CB' (ϵ'_{CB}, f'_{CB}) to the point CC' ($\epsilon'_{CC}, f'_{CC} = 0$). Reloading in tension after the stress-strain segment $C3$ follows the line $CC-TB$ (i.e., denoted as segment $C4$), where TB (ϵ_{TB}, f_{TB}) is the last unloading point in the tensile stage (or take point TA if no unloading has occurred in the tensile stage). The unloading path from a point on the tensile envelope is dependent on the maximum historical compressive strain and remains the same as in Belarbi and Hsu [1994]. Specifically, when the absolute value of this strain is smaller than that of CA (i.e., ϵ_0), the unloading path follows the segment $T3$ (from TB (ϵ_{TB}, f_{TB}) to TC (ϵ_{TC}, f_{TC})), $T4$ (from TC (ϵ_{TC}, f_{TC}) to TD (ϵ_{TD}, f_{TD}))), and then $C1$ sequentially. In contrast, when the absolute value of this strain is larger than that of CA (i.e., ϵ_0), the unloading path follows $T3'$ (from TB' to TC'), $T4'$ (from TC' to CB), then $C2$ sequentially. To summarize, the loading/unloading rules are expressed with the analytical expression of each loading path are given in Table 1. f^c and ϵ are the stress and the strain of any generic point in the loading path, respectively, while E_{CC} presents the secant stiffness of four segments (i.e., segments $C3$, $C4$, $T3$, and $T4$). Note that the unloading and reloading paths are on the same segment for intermediate stages unless either end-point of this segment (i.e., segment $C3$, $C4$, $T3$, or $T4$) has reached.

Table 1. The analytical expression of cyclic loading paths.

Loading path	The formula of the loading path
Segment C1	$f^c = (\xi f_c - f_{TD}) \left[2\epsilon/\epsilon_0 - (\epsilon/\epsilon_0)^2 \right] + f_{TD}$
Segment C2	$f^c = \xi f_c \left\{ 1 - [(\epsilon/\epsilon_0 - 1)/(4/\xi - 1)]^2 \right\}$
Segment C3	$f^c = f_{CB} + E_{CC}(\epsilon - \epsilon_{CB}) \text{ if } \epsilon_{CB} < \epsilon \leq \epsilon_{CC} \text{ else } E_{CC} = E_c$
Segment C4	$f^c = f_{CC} + E_{CC}(\epsilon - \epsilon_{CC}) \text{ if } \epsilon \leq \epsilon_{TB} \text{ where, } E_{CC} = (f_{TB} - f_{CC}) / (\epsilon_{TB} - \epsilon_{CC})$
Segment T1	$f^c = E_c \epsilon$
Segment T2	$f^c = f_{cr} (\epsilon_{cr}/\epsilon)^{0.4}$
Segment T3	$f^c = f_{TB} + E_{CC}(\epsilon - \epsilon_{TB}) \text{ if } \epsilon < \epsilon \leq \epsilon_{TB} \text{ where, } E_{CC} = (f_{TB} - f_{TC}) / (\epsilon_{TB} - \epsilon_{TC})$
Segment T4	$f^c = f_{TC} + E_{CC}(\epsilon - \epsilon_{TC}) \text{ if } \epsilon \leq \epsilon_{TC} \text{ where, } E_{CC} = (f_{TC} - f_{TD}) / \epsilon_{TC}$

In MCLM, the compression softening effect is considered in the same way as in Vecchio and Collins [1986], Belarbi and Hsu [1995], Pang and Hsu [1995], Hsu [1996], and Hsu and Zhu [2002], i.e., the compressive strength of one diagonal concrete bar is reduced by applying a softening coefficient ξ (see stages C1 and C2 in Fig. 3 and Table 1). In this model, ξ is determined by the tensile strain in the other diagonal bar. This study takes the same softening coefficient function ξ as proposed for the CSMM [Mansour *et al.*, 2001], i.e.,

$$\xi = \frac{5.8}{\sqrt{f'_c (\text{MPa})}} \frac{1}{\sqrt{1 + k\epsilon_r}} \leq 0.9 \quad (11)$$

where parameter k is taken as 400, f'_c is the compressive strength of concrete from cylinder tests, whose unit is MPa. It is important to point out that the softening coefficient function ξ in Equation (11) is used for computing the stresses of the two diagonal concrete bars. When calculating the two normal stresses, the coefficient ξ for compression softening is taken as a constant of 0.9 instead, i.e., assuming that the horizontal and vertical normal stresses are uncoupled.

2.3. The Tangent Moduli of the MCLM

In a FE analysis program, where Newton-Raphson (NR) method (or other gradient-based algorithms) is commonly used to solve nonlinear system of equations, the tangent stiffnesses (e.g., for the structure, the elements, and materials) are of significant importance. As such, the tangent moduli of the MCLM are derived herein. Following the stress computation process at a Gauss point, the tangent moduli of the MCLM, \mathbf{D} , is computed as in Equation (12),

$$\mathbf{D} = \frac{d\sigma}{d\epsilon} = \frac{d\sigma^s}{d\epsilon} + \frac{d\sigma^c}{d\epsilon} \quad (12)$$

According to Equation (2), the tangent moduli of the reinforcing steel layer can be computed as,

$$\frac{d\sigma^s}{d\epsilon} = \mathbf{T}(-\theta_1)\mathbf{D}_{s1}\mathbf{T}(\theta_1) + \mathbf{T}(-\theta_2)\mathbf{D}_{s2}\mathbf{T}(\theta_2) \quad (13)$$

where \mathbf{D}_{si} ($i = 1, 2$) is defined as,

$$\mathbf{D}_{si} = \begin{bmatrix} \rho_i E_{si} & 0 & 0 \\ 0 & 0 & 0 \\ 0 & 0 & 0 \end{bmatrix} \quad (14)$$

Here, $E_{si} = df_{\theta_i}^s/d\epsilon_{\theta_i}^s$ ($i = 1, 2$) is the tangent modulus of the uniaxial smeared reinforcing steel material model. For the concrete layer, the tangent moduli can be obtained from Equation (15),

$$\frac{d\sigma^c}{d\epsilon} = \begin{bmatrix} 0 & 0 & 0 \\ 0 & 0 & 0 \\ 0 & 0 & \zeta \end{bmatrix} \mathbf{T}\left(-\frac{\pi}{4}\right) \mathbf{D}_{c1} \mathbf{T}\left(\frac{\pi}{4}\right) + \mathbf{D}_{c2} \quad (15)$$

where \mathbf{D}_{c1} is the equivalent stiffness matrix obtained from the two diagonal concrete bars, as shown in Equation (16),

$$\mathbf{D}_{c1} = \begin{bmatrix} \partial f_1^c / \partial \epsilon_1^c & \partial f_1^c / \partial \epsilon_2^c & 0 \\ \partial f_2^c / \partial \epsilon_1^c & \partial f_2^c / \partial \epsilon_2^c & 0 \\ 0 & 0 & 0 \end{bmatrix} \quad (16)$$

Here, $\partial f_i^c / \partial \epsilon_j^c$ ($i, j = 1, 2$) represents the stiffness component of the diagonal concrete bars, i.e., the derivative of the stress along the axis of the i th concrete bar with respect to the strain along the axis of the j th concrete bar (Fig. 1(e)). This can be readily derived using the chain rule based on the analytical expressions summarized in Table 1 and thus not presented herein in detail. Note that the off-diagonal components of the equivalent stiffness matrix, i.e., $\partial f_1^c / \partial \epsilon_2^c$ and $\partial f_2^c / \partial \epsilon_1^c$ in Equation (16), are nonzero due to the softening effect, i.e., the compressive stress in one diagonal bar is affected by the tensile strain of the other diagonal bar through the compression softening coefficient ξ , as shown in the segments C1 and C2 in Table 1. In these cases (i.e., segments C1 and C2),

$$\frac{\partial f_i^c}{\partial \epsilon_j^c} = \frac{\partial f_i^c}{\partial \xi} \cdot \frac{\partial \xi}{\partial \epsilon_j^c} \quad (i \neq j) \quad (17)$$

where $\partial \xi / \partial \epsilon_j^c$ can be computed from Equation (11). In addition, the second item \mathbf{D}_{c2} in Equation (15), the stiffness matrix contributed from the horizontal and vertical concrete bars, can be expressed as,

$$\mathbf{D}_{c2} = \begin{bmatrix} df_l^c / d\epsilon_l^c & 0 & 0 \\ 0 & df_t^c / d\epsilon_t^c & 0 \\ 0 & 0 & 0 \end{bmatrix} \quad (18)$$

Note that the off-diagonal components in Equation (18) are zero since the compression softening effect is not considered and there is no coupling between these two bars.

3. Stress Resultants for Multilayer Shell Element

The newly developed MCLM is implemented in *OpenSees* and is used jointly with an existing multilayer shell element [Lu *et al.*, 2013] in *OpenSees* to model the nonlinear behaviors of RC shear walls in realistic building structures. As illustrated in Fig. 4(a), several different layers, including composite (i.e., concrete and steel) layers and pure concrete layers, exist in a shell element for concrete shear walls. The FE formulation

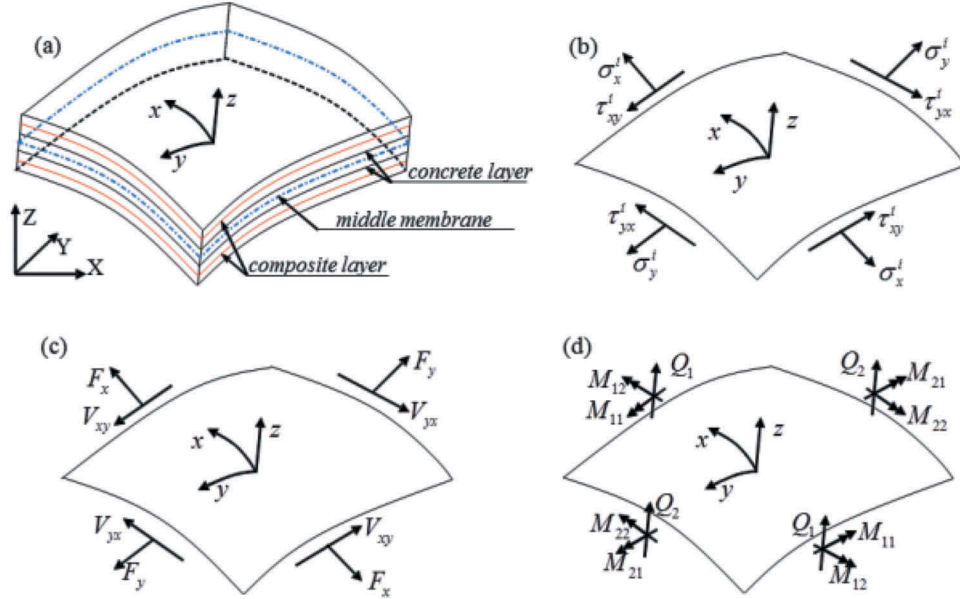


Figure 4. In-plane and out-of-plane stress resultants at a representative Gauss point of a 3D multilayer shell element: (a) a Gauss point of a multilayer shell element; (b) stresses calculated using MCLM for one concrete or composite layer at a Gauss point; (c) in-plane stress resultants (membrane forces); (d) out-of-plane stress resultants (moments and transverse shears).

of the shell element assumes that particles of the shell originally lying along a straight line (normal to the un-deformed middle membrane) remain aligned along a straight line during deformation [Bathe, 1996]. As such, the strain at each layer of a given Gauss point (i.e., four Gauss points per element) are calculated based on the displacement fields, which are interpolated using the nodal displacements. Both the composite and pure concrete layers are simulated using the MCLM, where the contribution of steel in Equation (2) is removed for pure concrete layers (e.g., by setting the reinforcement ratio ρ_i to be zero where $i = 1, 2$). The 2D stress resultants of each layer (i.e., σ_x^i, σ_y^i and τ_{xy}^i shown in Fig. 4(b)) at a Gauss point can be obtained based on the MCLM presented herein. Note that $\sigma_{zz} = 0$ due to the plane stress assumption in concrete shear walls.

At each Gauss point of the multilayer shell element, the stress resultants, including the membrane forces ($F_x, F_y, V_{xy} = V_{yx}$), moments (M_{11}, M_{22}, M_{12}) and transverse (i.e., out-of-plane) shear forces (Q_1, Q_2) can be calculated using the stresses at each layer [Hughes, 2000], according to Equations (19)–(21), respectively.

$$\begin{aligned} F_x &= \int_{-t/2}^{t/2} \sigma_x dz = \sum_{i=1}^N \sigma_x^i h_i, & F_y &= \int_{-t/2}^{t/2} \sigma_y dz = \sum_{i=1}^N \sigma_y^i h_i, \\ V_{xy} &= V_{yx} = \int_{-t/2}^{t/2} \tau_{xy} dz = \sum_{i=1}^N \tau_{xy}^i h_i \end{aligned} \quad (19)$$

$$\begin{aligned} M_{11} &= \int_{-t/2}^{t/2} \sigma_x z dz = \sum_{i=1}^N \sigma_x^i z_i h_i, \quad M_{22} = \int_{-t/2}^{t/2} \sigma_y z dz = \sum_{i=1}^N \sigma_y^i z_i h_i, \\ M_{12} &= \int_{-t/2}^{t/2} \tau_{xy} z dz = \sum_{i=1}^N \tau_{xy}^i z_i h_i \end{aligned} \quad (20)$$

$$Q_1 = \int_{-t/2}^{t/2} \mu \gamma_{xz} dz = \sum_{i=1}^N \mu \gamma_{xz}^i h_i, \quad Q_2 = \int_{-t/2}^{t/2} \mu \gamma_{yz} dz = \sum_{i=1}^N \mu \gamma_{yz}^i h_i \quad (21)$$

in which t is the entire thickness of the shear wall, N denotes the number of layers, h_i and z_i represent the thickness and z -coordinate of the i th layer, respectively, and μ indicates the shear module of concrete material.

4. Application Examples

Three RC shear wall specimens subjected to quasi-static cyclic loading conditions are used to validate the newly developed MCLM for the accuracy, as well as computational efficiency and numerical stability. Additionally, the newly developed MCLM is applied to a 129-meter 32-story high-rise RC frame-shear wall building subjected to earthquake ground motion excitation in order to illustrate its promising application to realistic high-rise RC structures. The modeling and simulation results for these application examples are presented as follows.

4.1. Example I: A RC Shear Wall with Flexural-Shear Deformations

A shear wall specimen, denoted as RW2, was tested in Thomsen and Wallace [2004]. This wall has a rectangular cross section and is 3660 mm tall and 102 mm thick, with a web length of 1220 mm. More details about this specimen can be found in Thomsen and Wallace [2004]. In this study, a FE model, consisting of two boundary columns and the middle panel as illustrated in Fig. 5, is developed in *OpenSees* using the newly implemented MCLM in order to simulate the cyclic responses of the specimen wall. Each boundary column is modeled using 10 displacement-based Euler-Bernoulli beam-column elements with RC fiber sections of 153 mm in width and 102 mm in height (see Fig. 5(b)). The concrete and steel fibers in the discretized section are represented using a modified Kent-Park-Scott material model [Park *et al.*, 1982], shown in Fig. 5(d), and a Giuffre-Menegotto-Pinto material model [Menegotto, 1973; Filipou *et al.*, 1983], shown in Fig. 5(e), respectively. Different material parameters are used for the confined (i.e., “core”) and unconfined (i.e., “cover”) concrete to account for the confinement effect of stirrups. The model parameters of the concrete constitutive models and steel reinforcement model are summarized in Table 2. The concrete model parameters are: f_c = the peak strength of concrete in compression; f_u = the residual strength of concrete in compression; ϵ_0 = the strain at peak strength; ϵ_u = the strain at which the residual strength is reached; b = the ratio between unloading slope at ϵ_u and the initial stiffness E_0 ; f_t = the tensile strength of concrete; and E_t = the absolute value of tension softening stiffness. The steel model parameters for the Giuffre-Menegotto-Pinto model are: E = the Young’s modulus; f_y = the yield strength; and b = the post-yield strain-hardening ratio.

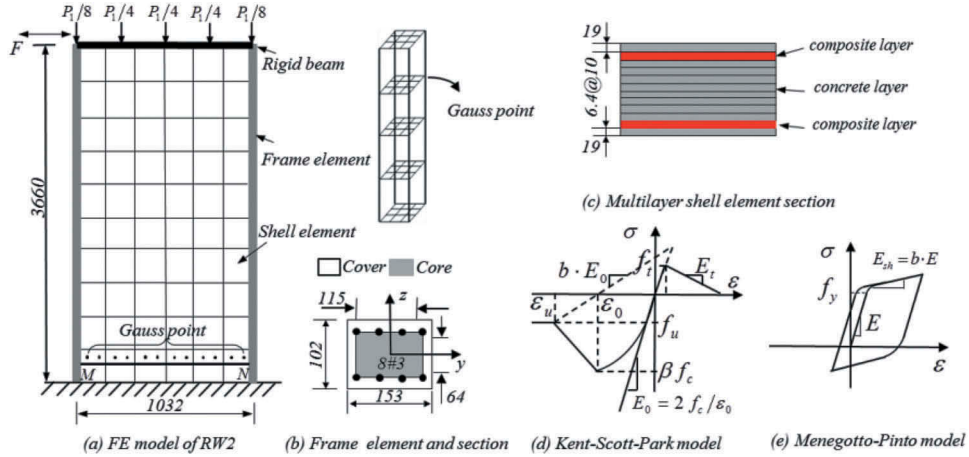


Figure 5. FE model, frame and shell elements, and concrete and steel constitutive models for RW2 (length units: mm).

The middle panel is modeled by using 60 four-node multilayer shell elements each with four Gauss points, and the MCLM used to simulate the nonlinear hysteretic behaviors of each layer (see Fig. 5(c)). Modeling parameters for the MCLM in the composite layer and the pure concrete layer are summarized in Table 2, where ρ_l and ρ_t are the reinforcement ratio in the horizontal and vertical directions, respectively; f_c denotes the peak strength of concrete in compression; and ε_0 is the strain at peak strength (see Fig. 3 and Table 1). Note that the nodes of shell elements and beam-column elements both have the same (6) degrees of freedom; thus these two types of elements share the same nodes at the same location at their boundary herein.

The test specimen were subjected to cyclic loading conditions by imposing the same displacement history at the top as detailed in Thomsen and Wallace [2004] after a uniformly distributed vertical load (i.e., $P_1 = 3.78 \times 10^5$ N corresponding to the axial force ratio of about 0.07). Therefore, the FE model subjected to cyclic loading conditions is analyzed by using a displacement control method after a load control analysis with equivalent nodal forces applied at the top as shown in Fig. 5. The comparisons between experimental and predicted responses, including the shear force versus top displacement, the lateral deformation profile, concrete strains at the base of the wall, steel strains at the base and first-story levels are presented in Figs. 6–10.

Table 2. Modeling parameters of the FE model for RW2 (units of strengths and Young's modulus: MPa).

1D Concrete Para. For Column	ε_0	ε_u	f_c	f_u	b	f_t	E_t
Core	0.0033	0.015	47.6	33	0.1	2.6	3.0e3
Cover	0.0021	0.0115	42.8	8.2	0.1	2.6	3.0e3
1D Steel Para. for Column	E_0	f_y	b	R0	cR1	cR2	
Steel02 in OpenSees	2.0e5	448	0.0005	18	0.925	0.15	
2D MCLM	θ_1	θ_2	ρ_l	ρ_t	f_c	ε_0	f_y
Composite layer	0	$\pi/2$	3.825%	3.825%	42.8	0.0021	336
Concrete layer	0	$\pi/2$	—	—	42.8	0.0021	—

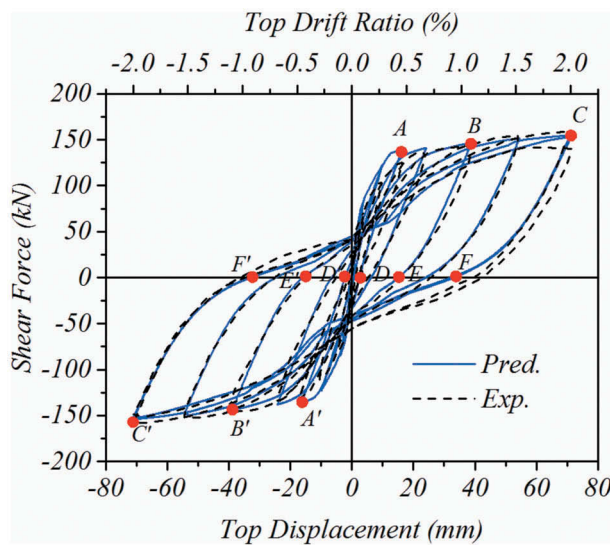


Figure 6. Comparison between predicted and experimental hysterical responses for RW2.

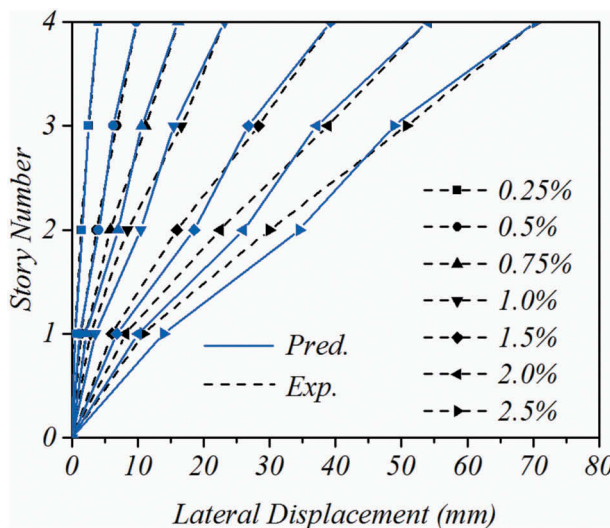


Figure 7. Comparisons of the lateral displacement profiles between experimental and predicted results for RW2.

Fig. 6 shows the comparison between predicted and experimental hysterical responses (i.e., base shear force versus top displacement) for RW2. Compared with the experimental results as shown in Fig. 6, the relative prediction errors of the shear forces at points A, B, C, A', B', and C' are 11.6%, 5.5%, 9.5%, 5.7%, 2.2%, and 3.0%, respectively. The predicted plastic displacement at D, E, F, D', E', and F' (i.e., the residual plastic displacement when unloading from the points A, B, C, A', B' and C') are 2.7 mm, 15.5 mm, 32.8 mm, -2.6 mm, -16 mm, and -34.4 mm, respectively, corresponding to relative prediction errors of 18.5%, 2.6%, 15.8%, 20%, 6.3%, and 4.2%, respectively. On the other hand, the

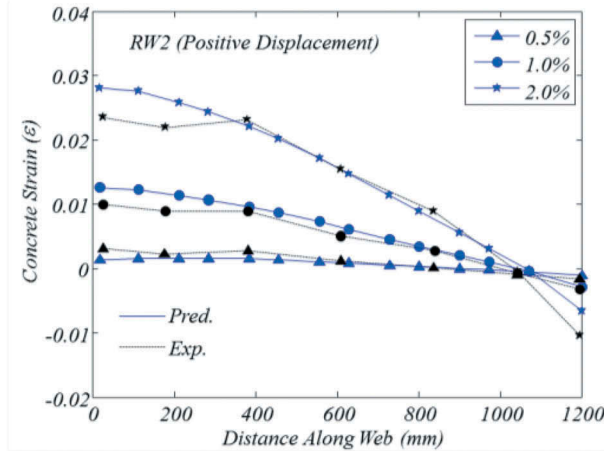


Figure 8. Comparison between concrete strains measured by LVDTs and corresponding predicted strain for RW2.

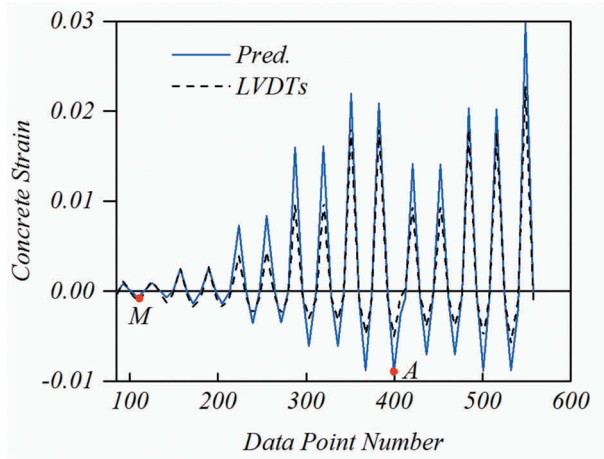


Figure 9. Comparison between concrete strains measured by LVDTs and corresponding predicted strain for RW2.

hysteretic energies dissipated are $4.65\text{e}4$ J and $5.07\text{e}4$ J, respectively, from the prediction (with a relative error of 8%) and the experiment. Overall, it can be observed from Fig. 6 that the hysteretic behaviors (i.e., the stiffness degradation, the plastic displacements, and the pinching behaviors) of the RC shear wall under flexural-shear deformations can be simulated by the FE model using the MCLM with acceptable accuracy.

Fig. 7 compares the experimental and predicted deformation profiles of the shear wall corresponding to various top drift levels (i.e., 0.25%, 0.5%, 0.75%, 1.0%, 1.5%, 2.0%, and 2.5%). A good agreement is observed when the lateral drift level is low (e.g., less than 0.5%), while the discrepancy slightly increases with increasing lateral drift ratios. Overall, the simulated lateral deformation profile and the deformation distribution pattern have acceptable accuracy.

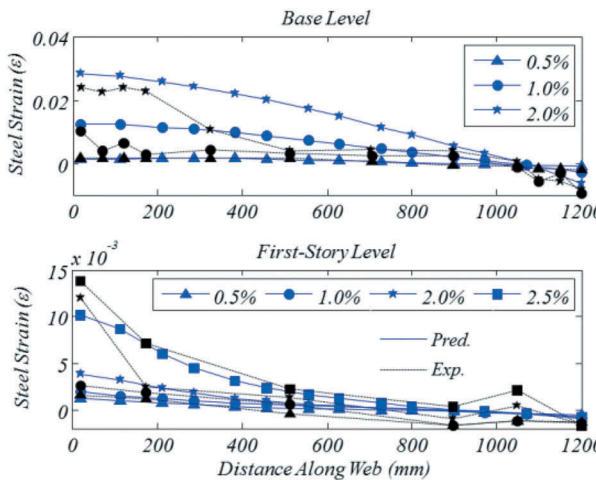


Figure 10. Comparison between steel strains measured by strain gages and corresponding predicted strain for RW2.

In addition to the global response quantities shown in Figs. 6 and 7, local response quantities are also compared for this specimen. Fig. 8 plots the average concrete strains measured by seven linear variable differential transducers (LVDTs) over a gage length of 229 mm at the base of the wall (see the line MN in Fig. 5), at three different top drift ratio levels (i.e., 0.5%, 1.0%, and 2.0%). The calculated concrete strains at different locations along the web agree well with the corresponding measurements when the top drift is 0.5%, and the measured and simulated tensile strains along the web distance are almost linear. The agreement becomes slightly worse with the increase of the top drift ratio. When the magnitude of the top drift ratio is 2.0%, the predicted concrete strains at locations along the web between 400 mm and 1000 mm are almost linear, and they match well with the experimental ones. The tensile strains measured by the LVDTs in the other part (e.g., 0–400 mm) can possibly be polluted by the cracks in this region of the shear wall specimen. To sum up, the overall predicted concrete strains have acceptable agreement with the experimental data.

To have a closer look at concrete strains predicted by the FE model, Fig. 9 presents the comparisons between predicted concrete strains and those measured by LVDTs (see Line MN in Fig. 5). The data points indicate concrete strains at different top drift levels: the data points from No. 1 to No. 195 are corresponding to the top drift level of 0.5%, while the consequential points from No. 196 to No. 550 are corresponding to the top drift level of 0.75% to 1.0%, 1.5%, 2.0%, and 2.5%. As seen from the comparison for data points from No. 1 to No. 195, the predicted concrete strain responses are slightly smaller than the experimental results measured by the LVDTs with the maximum relative prediction error of 25% at point M (see Fig. 9) when the shear wall specimen experiences weak nonlinearities. In contrast, while the shear wall specimen experiences strong nonlinearities with the drift level increasing from 0.75% to 2.5%, the predictions are larger than the measurements with the maximum relative prediction error of 40% at point A (see Fig. 9). A possible explanation for such prediction error is that a large number of cracks concentrate in the regions slightly above the first story instead of at the bottom of the

specimen as indicated by Fig. 7, and the stress redistribution leads to the reduction of the strain at the bottom region. However, the FE model calculates an average or ‘homogenized’ strain that cannot simulate accurately the actual local cracks and stress redistributions, yielding larger concrete strains in this example. Note that the model error can be possibly traced back to the poor assumption made about the rigid boundary conditions at pedestal base, which in reality is not rigidly connected to the wall panel.

Fig. 10 shows the comparisons between steel strains measured by strain gages and corresponding predicted strains at the base and the first-story levels. Similar to the concrete strains discussed above, good predictions for the tensile strain at both the base and the first-story levels are obtained when the top drift ratio is low (e.g., 0.5%). However, the discrepancy increases when the top drift ratio increases. The experimental steel strains show strong nonlinear behaviors at left region (i.e., about 0–200 mm) and right region (i.e., about 1,000–1,200 mm) along the web. However, the predicted ones are almost linearly distributed along the web. The potential sources of the discrepancies are: (1) the slip between concrete and steel in FE model is neglected, (2) a smeared crack model for concrete and a smeared steel model are applied, (3) a smooth shape function is used in approximating the displacement of FE elements. Therefore, the FE analysis predicts only ‘homogenized’ or ‘average’ strains, and thus cannot accurately simulate the actual non-uniformly distributed crack distributions (and actual non-uniform strain) of the concrete and steel.

In order to investigate the computational efficiency and numerical stability of the MCLM, the convergence performance is studied. A tolerance of 1.0e-5 N on the norm of the unbalanced force vector is used as the convergence criterion in the analyses. Fig. 11 shows a percentage representation of the number of iterations required for convergence during analysis for the cyclic loading. The total number of iterations for the load steps is 57,974 and the average number of iterations for convergence is about 2.6. In most of load steps, the NR process requires 3 or 2 iterations for convergence, accounting for 59.5% and 39.7% of the total number of iterations, respectively. The maximum number of iterations required for

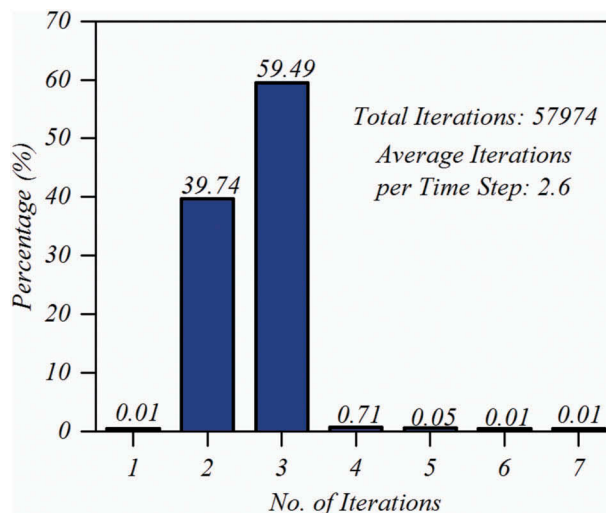


Figure 11. Percentage representation of the numbers of iterations required for convergence for RW2.

Table 3. Norm of residual unbalance force vectors versus iterations for six representative load steps with varying number of iterations required for convergence.

Iterations	2	3	4	5	6	7
No. of Iteration = 1	2.0e-4	2.0e-4	3.8e-3	1.3e-3	3.8e-3	2.7e-2
No. of Iteration = 2	3.2e-6	5.2e-005	3.7e-3	1.0e-3	2.0e-3	1.9e-2
No. of Iteration = 3		7.7e-010	3.1e-5	2.4e-4	6.0e-4	4.6e-3
No. of Iteration = 4			5.0e-9	1.4e-5	1.2e-4	1.3e-3
No. of Iteration = 5				4.6e-9	3.0e-5	6.4e-4
No. of Iteration = 6					4.1e-8	2.2e-5
No. of Iteration = 7						3.4e-8

convergence is 7 (accounting for 0.01% of the total number of iterations). A closer investigation is conducted for six representative load steps, which required the numbers of iterations for convergence from 2 to 7 (see **Table 3**). It is observed that the NR process for the FE model using MCLM converges quadratically for most of the cases. Generally, 2 to 5 iterations are required per load step. **Fig. 11** implies that the computational time for the ‘slow convergence’ cases accounts for about 2% of the total calculation time. Therefore, the MCLM exhibits good computational efficiency and numerical stability in the example.

To sum up, the newly developed MCLM can simulate the flexural-shear behavior of typical shear wall specimens with acceptable accuracy and good efficiency, when the walls experience moderate nonlinearities as demonstrated in example I. Example II will be used to investigate the modeling capability of MCLM for shear walls that experience strong nonlinearities and subject to shear failures.

4.2. Example II: A RC Shear Wall with Shear Failure

A RC shear wall specimen (denoted as RW-A15-P10-S51), which is 1,829 mm tall, 153 mm thick, and 1,219 mm wide, was tested by Tran and Wallace [Tran and Wallace, 2012; Kolozvari *et al.*, 2015]. Details on sections, reinforcements and material properties are not elaborated herein and can refer to Panagiotou *et al.* [2012] and Kolozvari *et al.* [2015]. This specimen is similar to the specimen in example I and thus a FE model is developed with the same modeling scheme as shown in **Fig. 12**, except the different meshing (i.e., 8 displacement-based Euler-Bernoulli fiber frame elements for each boundary column and 48 four-node shell elements for the middle shear panel). The material model parameters are listed in **Table 4**.

The test specimen were subjected to cyclic loading conditions by imposing a displacement history at the top (the detail loading path is defined in Tran and Wallace [2012]) after a uniformly distributed vertical load (i.e., axial force ratio = 0.077). Therefore, the FE model subjected to the same cyclic loading conditions is analyzed by using a displacement control method after a load control analysis with equivalent nodal forces applied at the top as shown in **Fig. 5** with $P_1 = 699$ kN. The comparisons between experimental and predicted responses, including the shear force versus top displacement, the lateral deformation profile, concrete strains at the base of the wall, steel strains at the base and first-story levels, are presented in **Figs. 13 and 14**.

Fig. 13 shows the comparison between experimental and predicted hysteretic responses (i.e., base shear force versus top displacement). The shear wall specimen experiences three stages denoted as stages I, II, and III, respectively. Stage I involves small nonlinearity ranging from the origin to P_1 and P_1' , with the corresponding plastic displacements at Q_1

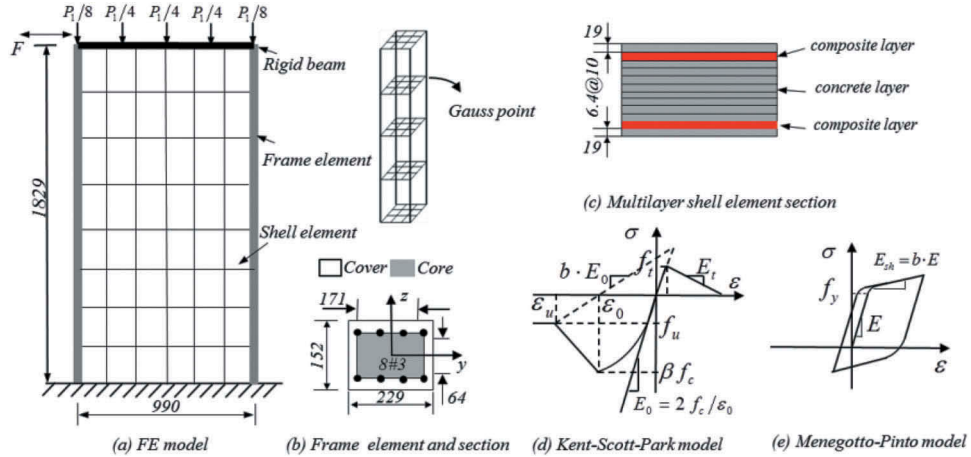


Figure 12. FE model, frame and shell elements, and material constitutive models for RW-A15-P10-S51 (length units: mm).

Table 4. Modeling parameters of the FE model for RW-A15-P10-S51 (units of strengths and Young's modulus: MPa).

1D Con. Para.	ε_0	ε_u	f_c	f_u	b	f_t	E_t
Core Con.	0.0056	0.028	63.9	48.7	0.1	2.16	3.0e3
Cover Con.	0.0022	0.01	48.7	9.74	0.1	2.16	3.0e3
1D Steel Para.	E_0		f_y		b	R0	cR1
Steel02	2.0e5		472.7		0.01	18	0.925
2D MCLM	θ_1	θ_2	ρ_l	ρ_t	f_c	ε_0	f_y
Composite layer	0	$\pi/2$	5.1%	5.1%	42.8	0.002	450.2
Concrete layer	0	$\pi/2$	–	–	42.8	0.002	–

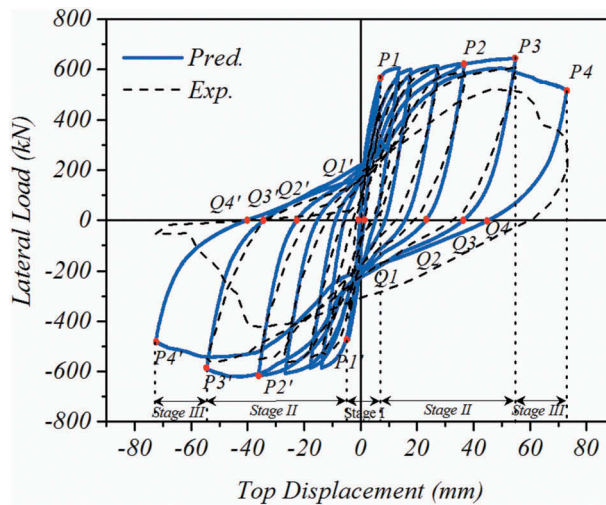


Figure 13. Comparison between predicted and experimental hysterical responses for RW-A15-P10-S51.

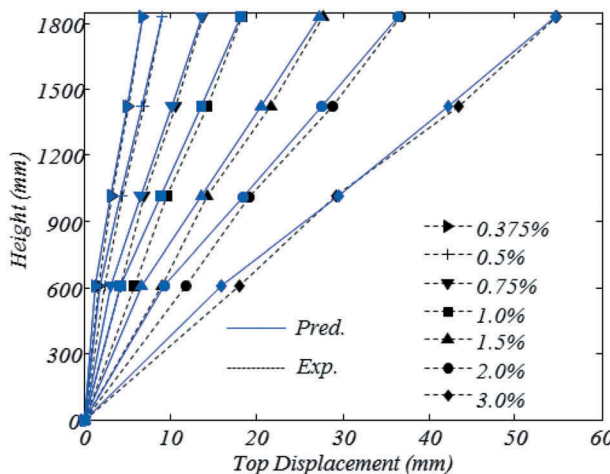


Figure 14. Comparisons of the lateral deformation profiles between experimental and predicted results for RW-A15-P10-S51.

and $Q1'$ equal to 2.3 mm and -2.4 mm, respectively. When compared with the experimental results, the relative prediction errors for the shear forces at points $P1$ and $P1'$ are 8.2% and 10%. The relative prediction error for the plastic placements at $Q1$ and $Q1'$ are 20% and 19%. The predicted responses agree with the experimental ones with acceptable accuracy in the stage I. The stage II, ranging from $P1$ to $P3$ and from $P1'$ to $P3'$ (see Fig. 13), in which the specimen experiences moderate to strong nonlinearities. During stage II, the relative prediction error for the shear forces at points $P2$, $P3$, $P2'$, and $P2'$ are 5.4%, 3.9%, 10%, and 3.9%, respectively. The relative prediction errors for the corresponding plastic displacements at $Q2$, $Q3$, $Q2'$, and $Q3'$ are 13.6%, 13.7%, 14.8%, and 7.8%. The relative prediction errors are practically acceptable in Stage II. The Stage III denotes the damage stage, i.e., ranging from $P3$ to $P4$ and $P3'$ to $P4'$. In stage III, serious stiffness and strength degradation due to the shear failure are observed, and brittle failure occurred suddenly in the experiment. The predicted plastic displacements at $Q4$ and $Q4'$ are 43.7 and -43.0 mm, respectively. The relative prediction errors for the shear forces at points $P4$ and $P4'$ are 37% and 88%, and the relative prediction errors for the plastic placement at $Q4$ and $Q4'$ are 27% and 5%. Note that the predicted responses can provide only qualitative description about the damage in this stage. The dissipated hysteretic energies are computed from the global lateral force versus top flexural displacement in the Fig. 13. In stage I and stage II, the total energy dissipations are $1.086e5$ J and 1.048 J, respectively, when estimated from predicted (with relative prediction errors less than 3%) and experimental hysteretic curves. However, when the specimen experiences a dramatic shear failure in stage III, the energies dissipated are $2.044e5$ J and $1.626e5$ J, respectively, when estimated from predicted and experimental hysteretic curves. The relative prediction error increases to approximately 20%. Note that the analysis results show that the hysteretic behavior (i.e., the stiffness degradation, the plastic displacements, and the pinching behaviors in the Stages I, II and III) can also be simulated by using the MCLM for the shear wall specimen, which is subject to 'extreme' shear failure loading conditions, with practically acceptable accuracy.

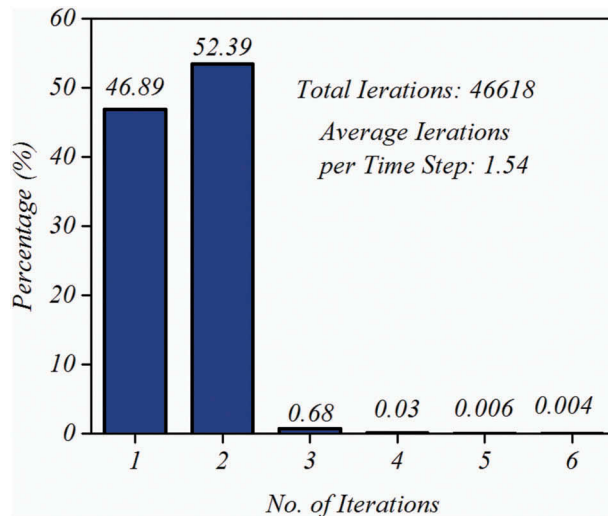


Figure 15. Percentage representation of the numbers of iterations required for convergence for RW-A15-P10-S51.

Fig. 14 shows the comparison of the lateral deformation profiles between experimental and predicted results. Similar observations can be made that the prediction agrees well with the experimental results when the lateral drift ratio is low (i.e., less than 0.75%), while the discrepancy slightly increases with the increase of lateral drift ratio. Overall, the simulated lateral deformation profile and the deformation distribution pattern have acceptable accuracy.

During the analysis, a tolerance of 1.0e-5 N on the norm of the unbalanced force vector is used as convergence criterion. Fig. 15 shows a percentage representation of the iteration numbers required for convergence during analysis for the cyclic loading. The average number of iterations for convergence is 1.54, i.e., the NR process requires 1 or 2 iterations for convergence, accounting for 46.89% and 52.39% of the total number of iterations, respectively. The maximum number of iteration required for convergence is 6 (but it is very rare). Table 5 shows the numbers of iterations required for convergence at six representative load steps. It is observed that the quadratic convergence rate is achieved for most of the cases in which 1 to 5 iterations are required per load step. Therefore, this example further confirms the good computational efficiency and numerical stability of the MLCM.

Table 5. Norm of residual unbalance force vectors versus iterations at six representative load steps with varying number of iterations required for convergence for RW-A15-P10-S51.

Iteration	1	2	3	4	5	6
No. of Iteration = 1	2.0e-7	2.7e-4	5.8e3	1.8e4	2.e4	2.7e3
No. of Iteration = 2		2.4e-8	5.3e-4	8.6e2	1.7e3	4.3e2
No. of Iteration = 3			8.4e-8	2.8	355.4	4.8e1
No. of Iteration = 4				8.7e-8	0.37	0.89
No. of Iteration = 5					3.0e-7	1.9e-5
No. of Iteration = 6						1.3e-7

4.3. Example III: A 3D T-Shaped Shear Wall

3D shear walls, such as T-shaped shear walls, are commonly used components in core-tube shear-wall buildings in practice. In order to further validate the applicability of the proposed MCLM for 3D RC shear walls, a tested T-shaped shear wall component in Orakcal and Wallace [2006] and Lu and Panagiotou [2014], denoted as TW2 herein, is used. The height of the T-shaped wall is 3,660 mm; the lengths of both the web and the flange of this wall are 1,219 mm; and the thicknesses of both the web and the flange are 102 mm. More details on reinforcement, concrete and steel parameters can be found in Orakcal and Wallace [2006] and Lu and Panagiotou [2014]. The FE model for this shear wall is built in *OpenSees* following the same modeling scheme as depicted in Fig. 16. The web and flange are modeled using 32 four-node multilayer shell elements with four Gauss points for each element, respectively, and the MCLM for each composite or concrete layer (see Fig. 16(b)) of the shell element. Material modeling parameters for the boundary columns and the web/flange panels of TW2 are summarized in Table 6.

The same loading protocol is used for the analysis as the experiment performed by Orakcal and Wallace (2006) and Lu and Panagiotou (2014). Namely, after a uniformly distributed vertical load $P\$146\# = -787.6$ kN (i.e., 0.074 axial force ratio) was applied on the top of the specimen, the model was analyzed under cyclic loading conditions by using a displacement control method. The comparison between predicted and experimental hysterical responses (i.e., shear force versus top displacement) is presented in Fig. 17. Good correlation between the experimental and predicted hysteretic behaviors is achieved, especially in the positive direction. In contrast, the predicted initial stiffness and strength are slightly larger than experimental ones in the negative direction. The dissipated hysteretic energies are 7.43e4 J and 6.76e4 J, respectively, when calculated from the predicted (with a relative prediction error of 9%) and experimental hysteretic curves. Fig. 18 shows the comparisons of the lateral

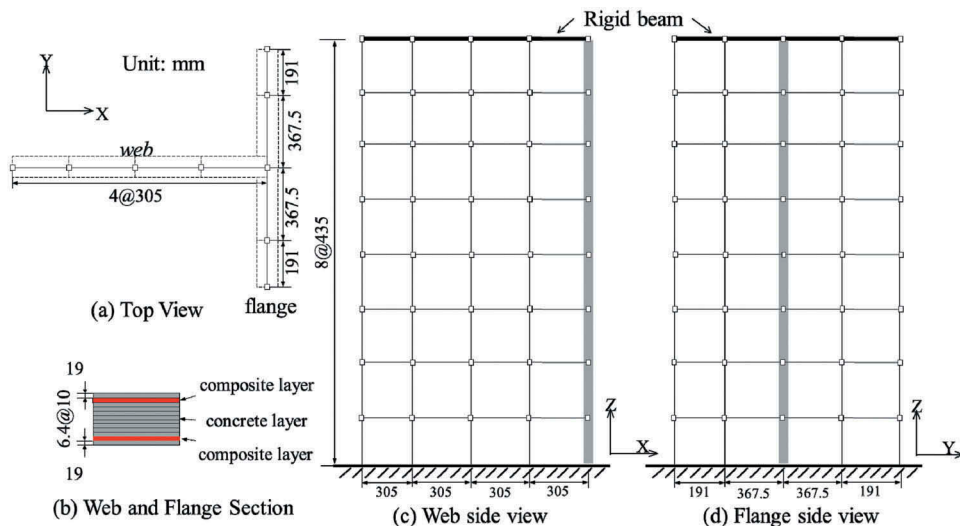
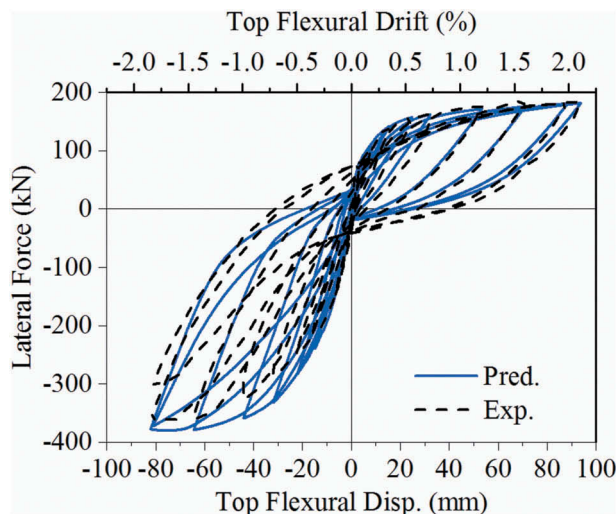
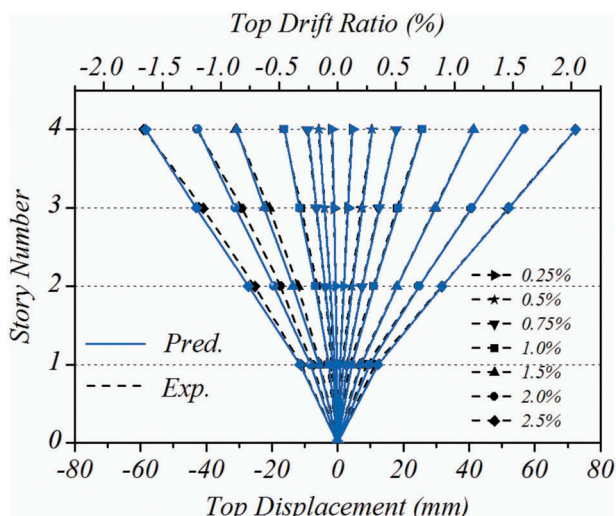


Figure 16. FE model of T-132#shaped wall, TW2.

Table 6. Modeling parameters of the FE model for TW2 (units of strengths and Young's modulus: MPa).

1D Con. Para.	ε_0	ε_u	f_c	f_u	b	f_t	E_t
Core Con.	0.006	0.02	53.8	43.0	0.1	2.6	3.0e3
Cover Con.	0.002	0.02	42.8	8.3	0.1	2.6	3.0e3
1D Steel Para.	E_0		f_y		b	R_0	$cR1$
Steel02	2.0e5		448		0.0005	18	0.925
2D MCLM	θ_1	θ_2	ρ_l	ρ_t	f_c	ε_0	f_y
Composite layer	0	$\pi/2$	7.0%	19.1%	42.8	0.002	448
Concrete layer	0	$\pi/2$	-	-	42.8	0.002	-

**Figure 17.** Comparison between predicted and experimental hysterical responses, TW2.**Figure 18.** Comparisons of the lateral deformation profiles between experimental and predicted results, TW2.

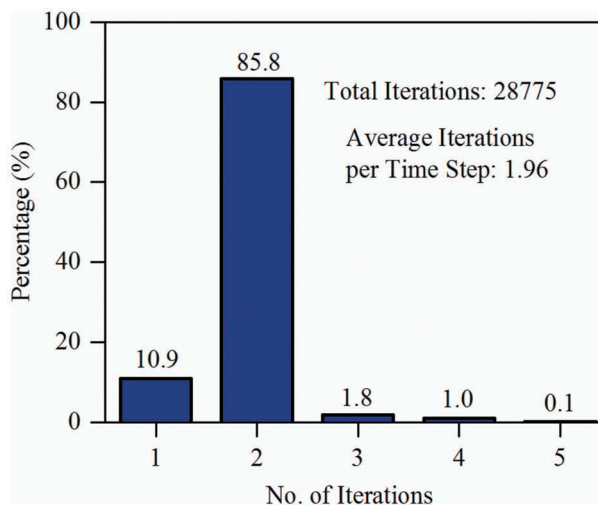


Figure 19. Percentage representation of the numbers of iterations needed for NR convergence, TW2.

deformation profiles between experimental and predicted results. The predicted responses have a good agreement with the experimental ones when the drift ratio is less than 1.0%, though the discrepancy between them slightly increases in the negative direction with the increase of drift ratio. Such results indicate that the FE model using MCLM can also be applied to 3D shear walls.

During the analysis of this 3D shear wall, the convergence criterion is set with a tolerance of 1.0e-3 mm imposed on the norm of the incremental displacement vectors. Fig. 19 shows a percentage representation of the number of iterations required for convergence during the analysis for the cyclic loading. The average number of iterations for convergence is 1.96, i.e., 1 or 2 iterations per load step for convergence, accounting for 10.9% and 85.8% of the total number of iterations, respectively. The maximum number of iterations required for convergence is 5 (accounting for 0.1% of total iterations). Table 7 shows the numbers of iterations required for convergence at five representative load steps. It is observed that the analysis converges quickly (typically after 1 or 2 iterations) for the 3D shear wall analysis. By virtue of its proved high efficiency and stability of the shear wall models using MCLM, a realistic high-rise building structure is modeled for nonlinear seismic analysis in the following section.

Table 7. Norm of residual unbalance force vectors versus iterations at six representative load steps with varying number of iterations required for convergence for TW2.

Iteration	1	2	3	4	5
No. of Iteration = 1	2.8e-4	5.6e-3	2.8e-2	1.2e-1	3.7e-2
No. of Iteration = 2		1.7e-5	4.5e-2	8.6e-2	2.5e-2
No. of Iteration = 3			4.97e-5	2.8e-3	8.2e-3
No. of Iteration = 4				8.7e-5	1.4e-3
No. of Iteration = 5					4.2e-4

4.4. Example IV: A 32 Story High-Rise Building

The newly developed MCLM is used to simulate the nonlinear seismic response of a 129-m 32-story high-rise RC frame-shear wall building (see Fig. 20(a)) [Sun *et al.*, 2018]. This is a realistic building structure designed according to the Chinese Code (GB 50011–2010 Code) for Seismic Design of Buildings with the seismic fortification intensity larger than 8 degrees. The building structure consists of core tube RC shear walls, outer steel-RC frames, outer steel beam and steel braces (see Fig. 20(b)). The building is 48 m in width, 48 m in length, and 129 m in height, consisting of the first story (5.0 m) and all the other 31 stories (4.0 m each). More details of component dimensions properties of the steel braces and beams, outer mega columns, shear walls, and coupling beams are summarized in Tables 8–12, respectively.

A FE model with 1920 nodes and 5696 elements is developed to simulate the nonlinear seismic behavior of this tall building. Each shear wall in the core tube is modeled by a multilayer shell element. The material parameters for the FE model refer to Table 8. The outer steel-RC frame columns, the outer steel beams, and the steel braces are modeled using displacement-based Euler-Bernoulli elements with fiber sections. The same uniaxial concrete and steel material models as in examples I and II are used for each fiber in the fiber section, i.e., the modified Kent-Park-Scott model [Park *et al.*, 1982] for both core and cover concrete fibers, and the Giuffre-Menegotto-Pinto model [Menegotto, 1973; Filipou *et al.*, 1983] for steel fibers. The dimensions of the structural components are depicted in Tables 9–12.

The density of concrete and steel are $2,700 \text{ kg/m}^3$ and $7,850 \text{ kg/m}^3$, respectively, and equivalent lumped masses are applied to the corresponding nodes in the model. The first three natural frequencies of the building are 0.4472, 0.6006, 0.6007 Hz, respectively. Gravity loads applied in the static analysis include: 5.0 kN/m^2 dead and live

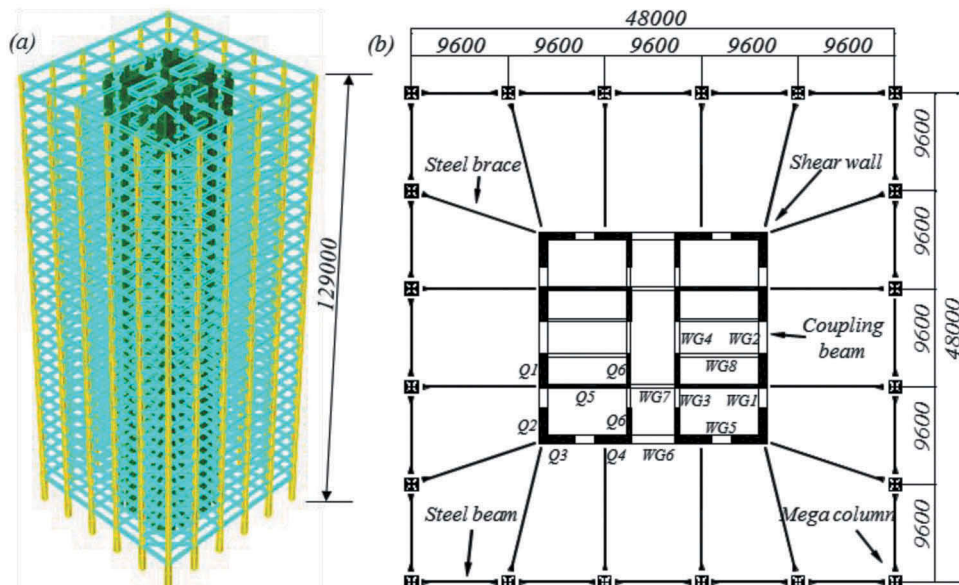


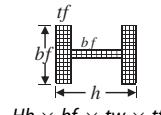
Figure 20. The 32-story RC frame-shear wall building (a) general view (b) one-story view (units of length: mm).

Table 8. Material properties of structural components in each story of the building (units of strength: MPa).

Component	Material	Compressive strength	Tensile strength
Floor 28 ~ 32: Shear wall/Column	C30	20.1	2.01
Floor 18 ~ 32: Plate			
Floor 21 ~ 27: Shear wall/Column	C40	26.8	2.39
Floor 1 ~ 17: Plate			
Floor 12 ~ 20: Shear wall/Column	C50	32.4	2.64
Floor 1 ~ 11: Shear wall/Column	C60	38.5	2.85
Steel beam	Q345	345	345
Reinforcement	HRB400	400	400

Table 9. Dimensions of the steel beams and braces.

Component	3F	4F~30F	31F~32F
Steel beam	H1200×350×22×30	H850×300×16×25	H850×300×16×25
Steel brace	H800×300×16×25	H850×300×16×25	-


Table 10. Dimensions of outer mega column (unit: mm).

Floor	1F~2F	3F~16F	17F~19F	20F~32F
Section	1200×1200	1000×1000	900×900	800×800
Reinforcement	40@25	32@25	24@22	24@22
Reinforced steel in X direction	H900×450×16×22	H700×350×16×20	H600×300×16×20	H500×250×16×20
Reinforced steel in Y direction	H900×450×16×22	H700×350×16×20	H600×300×16×20	H500×250×16×20

Table 11. Dimensions of shear wall in the core cube.

Floor	Q1	Q2	Q3	Q4	Q5	Q6
1F~4F	t/mm	800	800	800	350	350
	$\rho_l/\rho_t(\%)$	0.77/0.57	0.77/0.57	0.57/0.39	0.65/0.45	0.65/0.45
5F~10F	t/mm	700	700	700	350	350
	$\rho_l/\rho_t(\%)$	0.44/0.32	0.44/0.32	0.44/0.32	0.65/0.45	0.65/0.45
11F~19F	t/mm	600	600	600	300	300
	$\rho_l/\rho_t(\%)$	0.57/0.39	0.57/0.39	0.57/0.39	0.50/0.35	0.50/0.35
20F~32F	t/mm	450	450	450	300	300
	$\rho_l/\rho_t(\%)$	0.75/0.52	0.75/0.52	0.75/0.52	0.38/0.26	0.38/0.26
Width/mm	2800	2700	2700	3000	8500	2700

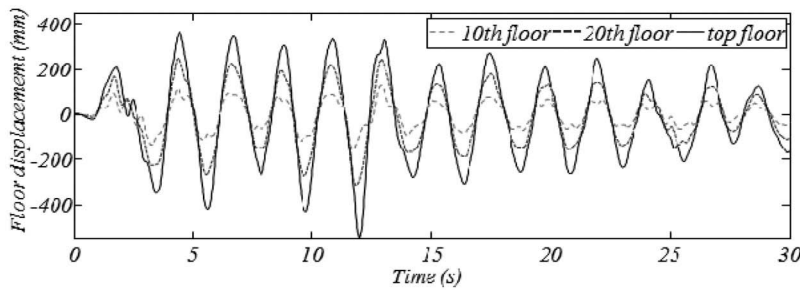
Note: parameter t denotes the thickness of the shear wall, ρ_l and ρ_t indicate horizontal vertical reinforcement.

load in the core cube area of each floor, respectively, while 4.5 kN/m^2 and 3.5 kN/m^2 in the other working areas, and 1.5kN/m^2 gravity load in the outer wall. After a quasi-static analysis for the model under these loads is performed, the 1940 El-Centro earthquake record scaled to a peak ground acceleration of 0.4 g is used as the base excitation input of the structural system. A numerical integration scheme, taking the Newmark- β integration with the parameters $\gamma = 0.5$ and $\beta = 0.25$ as an example, is employed, in which the numerical time step equals to 0.02 s . And the Rayleigh damping is used in the numerical model, where the damping ratios corresponding to the first-mode frequency and ninth-mode frequency (2.251 Hz) are 0.05 , respectively. A tolerance of $1.0\text{e-}3 \text{ mm}$ on the norm of the incremental displacement is adopted as the convergence criterion of the whole structural system. Fig. 21 shows the

Table 12. Dimensions of coupling beam in the core cube (unit: mm).

Floor		WG1	WG2	WG3	WG4	WG6	WG7	WG8	WG9
2F	Section	800×1200	800×1200	400×800	350×800	800×1200	800×1200	350×800	300×800
	Top	11@25	12@25	6@18	6@18	9@25	9@25	6@18	4@18
	Bottom	10@25	12@25	4@22	4@22	9@25	9@25	4@22	5@20
3F~5F	Section	800×1200	800×1200	350×800	350×800	800×1200	800×1200	350×800	300×800
	Top	16@25	23@25	6@25	5@25	11@25	12@25	6@20	4@18
	Bottom	16@25	22@25	5@25	5@25	11@25	11@25	4@22	5@20
6F~11F	Section	700×1200	700×1200	350×800	350×800	700×1200	700×1200	350×800	300×800
	Top	12@25	17@28	6@22	6@25	9@25	20@25	6@25	4@18
	Bottom	12@25	17@28	6@22	6@25	9@25	19@25	6@25	5@20
12F~20F	Section	600×1200	600×1200	400×800	300×800	600×1200	600×1200	300×800	300×800
	Top	8@25	14@25	4@25	5@22	8@22	16@25	6@25	4@18
	Bottom	7@25	14@25	4@25	5@22	6@25	15@25	5@25	5@20
21F~32F	Section	450×1200	450×1200	300×800	300×800	450×1200	450×1200	300×800	300×800
	Top	8@20	8@20	4@22	4@22	8@20	9@25	5@22	4@18
	Bottom	8@20	8@20	4@22	4@22	6@20	9@25	5@22	5@20
Width/mm		2500	4000	2500	4000	2800	4800	4800	8500

Note: Top and Bottom represent the top and bottom reinforcement of the coupling beam.

**Figure 21.** Displacement time histories of three representative stories.

displacement time histories of three representative floors and the magnitude of top displacement is 542.3 mm.

The hysteretic responses of the shear forces versus the drift ratios for representative shear walls at 1st, 10th, 20th, and 30th floors are studied and plotted in Fig. 22(a-d), respectively. It is observed that the maximum shear forces occur at the bottom of the structure and the shear forces decrease with elevation. The drift ratios initially increase and then decrease with elevation, and the maximum drift ratio occurs at around 20th floor. Similar high frequencies as in Fig. 22 are observed due to the high-frequency modes of the building during the earthquake. Furthermore, the FE model using the proposed MCLM jointly with the multi-layer shell elements exhibits good stability and converges systematically, which indicates that the newly developed RC shear wall model (i.e., MCLM) has a huge potential for practical use in the realistic high-rise shear-wall buildings.

5. Conclusions

This paper presents a novel practical MCLM to simulate RC shear walls under cyclic loadings. This model is validated using three tested shear wall specimens, and shows high numerical performance in terms of accuracy, efficiency, and stability, as well as its potential

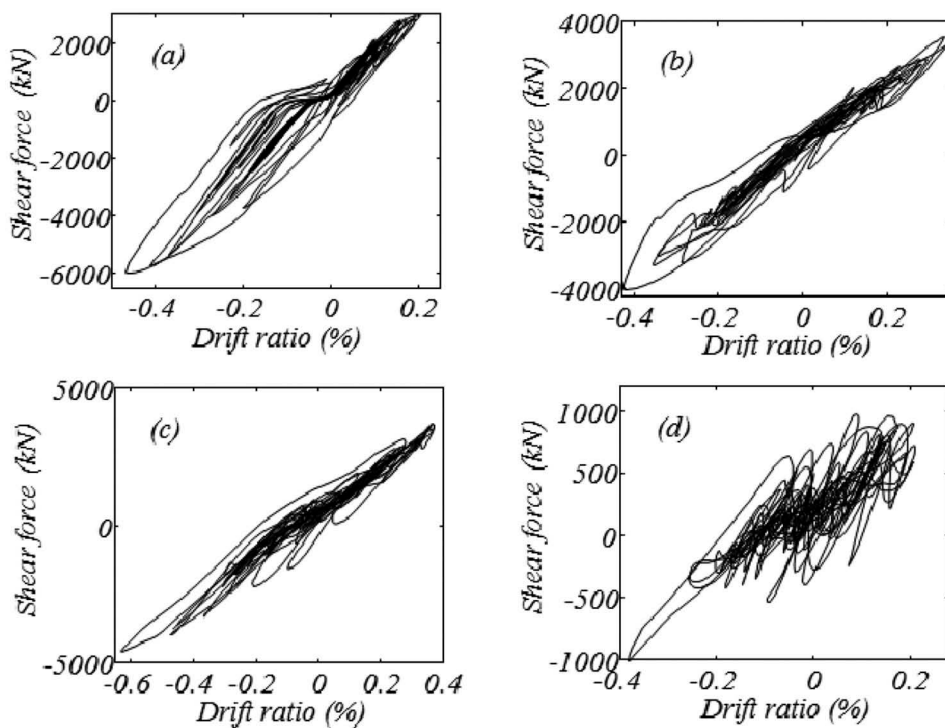


Figure 22. Shear force vs. drift ratio of shear walls in various floors (a) 1st floor, (b) 10th floor, (c) 20th floor, (d) 30th floor.

use for high-rise building structures. The MCLM combines concepts of micro- and macro-shear wall models by simulating the stress-strain relationship at material level (e.g., at a Gauss point) using a set of concrete or steel bars, and thereof calculating the resultant stress.

To be specific, the application of MCLM to two planar shear walls and one 3D T-shaped shear wall in this study show that the local and global responses, including the stiffness degradation, plastic displacements, and pinching behaviors, can be well captured when the shear walls are in linear or moderate nonlinear stages. For highly nonlinear cases, the predicted global responses (e.g., lateral forces versus displacement curves) agree with experimental ones, while the local responses (e.g., steel or concrete strains) exhibits relatively larger but reasonably acceptable discrepancies from a practical point of view. In addition to the accuracy, the convergence performance is assessed and good computational efficiency and numerical stability of the MCLM is demonstrated. To sum up, the MCLM is theoretically simple and practically convenient to use, relatively accurate, efficient, and stable; therefore, this study provides a practically useful tool for simulating the nonlinear behaviors of the RC shear walls in high-rise buildings during cyclic loadings (e.g., earthquakes).

Acknowledgments

Any opinions, findings, conclusions, or recommendations expressed in this publication are those of the authors and do not necessarily reflect the views of the sponsors.

Disclosure statement

No potential conflict of interest was reported by the author.

Funding

The authors acknowledge the financial supports from The National Key Research and Development Program of China with No. 2016YFC0701106, and from NSFC with No. 51261120376, 91315301-12, and 5157847. This paper is also supported by the Open Fund of Xiamen Engineering Technology Center for Intelligent Maintenance of Infrastructures [Grant No. TCIMI201801].

ORCID

Baoyin Sun  <http://orcid.org/0000-0002-6166-4535>

Yong Li  <http://orcid.org/0000-0003-0285-3069>

References

- Barbosa, A. R. [2011] "Simplified vector-valued probabilistic seismic hazard analysis and probabilistic seismic demand analysis: application to the 13-story NEHRP reinforced concrete frame-wall building design example," Ph.D. thesis, Dept. of Structural Engineering, University of California, San Diego.
- Bathe, K. [1996] *Finite Element Procedures*, Prentice Hall, Inc., Englewood Cliffs.
- Belarbi, A. and Hsu, T. T. C. [1994] "Constitutive laws of concrete in tension and reinforcing bars stiffened by concrete," *ACI Structural Journal* **91**(4), 465–474.
- Belarbi, A. and Hsu, T. T. C. [1995] "Constitutive laws of softened concrete in biaxial tension-compression," *ACI Structural Journal* **92**(5), 562–573.
- Fenves, G. L., Scott, M. H. and Takahashi, Y. [2004] "An object-oriented software environment for collaborative network simulation," *Proc. of the 13th World Conf. on Earthquake Engineering*, Vancouver, BC, Canada.
- Filipou, F. C., Popov, E. P. and Bertero, V. V. [1983]. "Effects of bond deterioration on hysteretic behavior of reinforced concrete joints." Report EERC 83-19, Earthquake Engineering Research Center, University of California, Berkeley.
- Hsu, T. T., Belarbi, A. and Pang, X. [1995] "A universal panel tester," *Journal of Testing and Evaluation* **23**(1), 41–49.
- Hsu, T. T., Mansour, M. Y., Mo, Y. L. and Zhong, J. [2006] "Cyclic softened membrane model for nonlinear finite element analysis of concrete structures," *Special Publication* **237**, 71–98.
- Hsu, T. T. C. [1993] *Unified Theory of Reinforced Concrete*, CRC Press, Inc, Boca Raton, Fla.
- Hsu, T. T. C. [1996] "Toward a unified nomenclature for reinforced concrete theory," *Journal of Structural Engineering* **122**(3), 275–283.
- Hsu, T. T. C. and Zhu, R. R. H. [2002] "Softened membrane model for reinforced concrete elements in shear *ACI Structural Journal* **99**(4), 460–469.
- Hughes, T. J. R. [2000] *The Finite Element Method: The Linear Static and Dynamic Finite Element Analysis*, Dover Publication, Mineola, NY.
- Kabeyasawa, T. [1997] "Design of RC shear walls in hybrid wall system," *Proc. of the Fourth Joint Technical Coordinating Committee, U.S.-Japan Cooperative Seismic Research on Composite and Hybrid Structures*, Monterey, CA.
- Kabeyasawa, T., Shiohara, H., Otani, S. and Aoyama, H. [1983] "Analysis of the full-scale seven-story reinforced concrete test structure," *Journal of the Faculty of Engineering* **37**(2), 431–478.

- Kolozvari, K., Tran, T. A., Orakcal, K. and Wallace, J. W. [2015] "Modeling of Cyclic Shear-Flexure interaction in reinforced concrete structural walls. II: experimental validation," *Journal of Structural Engineering* **141**(5), 04014136.
- Lu, X., Lu, X., Guan, H. and Ye, L. [2013] "Collapse simulation of reinforced concrete high-rise building induced by extreme earthquakes," *Earthquake Engineering & Structural Dynamics* **42**(5), 705–723.
- Lu, Y. and Panagiotou, M. [2014] "Three-dimensional cyclic beam-truss model for nonplanar reinforced concrete walls," *Journal of Structural Engineering* **140**(3), 04013071.
- Mansour, M. [2001] "Behavior of reinforced concrete membrane elements under cyclic shear: experiments to theory," Ph.D. thesis, Department of Civil and Environmental Engineering, University of Houston, Houston, TX.
- Mansour, M. and Hsu, T. T. C. [2005a] "Behavior of reinforced concrete elements under cyclic shear. I: experiments," *Journal of Structural Engineering* **131**(1), 44–53.
- Mansour, M. and Hsu, T. T. C. [2005b] "Behavior of reinforced concrete elements under cyclic shear. II: theoretical model," *Journal of Structural Engineering* **131**(1), 54–65.
- Mansour, M., Lee, J. Y. and Hsu, T. T. C. [2001] "Cyclic stress-strain curves of concrete and steel bars in membrane elements," *Journal of Structural Engineering* **127**(12), 1402–1411.
- McKenna, F., Scott, M. H. and Fenves, G. L. [2009] "Nonlinear finite-element analysis software architecture using object composition," *Journal of Computing in Civil Engineering* **24**(1), 95–107.
- Mckenna, F. T. [1997] "Object-oriented finite element programming: frameworks for analysis, algorithms and parallel computing," Ph.D. thesis, Civil & Environmental Engineering, University of California, Berkeley.
- Menegotto, M. [1973] "Method of analysis for cyclically loaded RC plane frames including changes in geometry and non-elastic behavior of elements under combined normal force and bending," *Proc. of the Symp. Resistance and Ultimate Deformability of Struct. Acted on by Well-Defined Repeated Loads*, IABSE Reports, Zurich, Switzerland.
- Moharrami, M., Koutromanous, I., Panagiotou, M. and Girgin, S. C. [2015] "Analysis of shear-dominated RC columns using the nonlinear truss analogy," *Earthquake Engineering & Structural Dynamics* **44**(5), 677–694.
- Orakcal, K. and Wallace, J. W. [2006] "Flexural modeling of reinforced concrete walls-experimental verification," *ACI Structural Journal* **103**(2), 196–206.
- Panagiotou, M., Kim, G., Barbosa, A. and Restrepo, J. I. [2009]. "Response verification of a reinforced concrete bearing wall building located in an area of high seismic hazard." Rep. prepared for the Portland Cement Association. Skokie, IL.
- Panagiotou, M., Restrepo, J. I., Schoettler, M., Geonwoo, K., Schoettler, M. and Geonwoo, K. [2012] "Nonlinear Truss model for reinforced concrete walls," *ACI Structural Journal* **109**(2), 205–214.
- Pang, X. B. and Hsu, T. T. C. [1995] "Behavior of reinforced concrete membrane elements in shear," *ACI Structural Journal* **92**(6), 665–679.
- Pang, X. B. and Hsu, T. T. C. [1996] "Fixed angle softened truss model for reinforced concrete," *ACI Structural Journal* **93**(2), 197–207.
- Park, H. and Eom, T. [2007] "Truss model for nonlinear analysis of RC members subject to cyclic loading," *Journal of Structural Engineering* **133**(10), 1351–1363.
- Park, R., Priestley, M. J. and Gill, W. D. [1982] "Ductility of square-confined concrete columns," *Journal of the Structural Division* **108**(4), 929–950.
- Sun, B., Gu, Q., Zhang, P. and Ou, J. [2018] "A practical multi-cross-line model for simulating nonlinear cyclic behavior of reinforced concrete shear wall in super high-rise buildings," in *Experimental Vibration Analysis for Civil Structures. EVACES 2017*, eds. J. Conte, R. Astroza, G. Benzoni, G. Feltrin, K. Loh and B. Moaveni (Lecture Notes in Civil Engineering, Springer, Cham), pp. 364–375.
- Thomsen, J. H. and Wallace, J. W. [2004] "Displacement-based design of slender reinforced concrete structural walls-experimental verification," *Journal of Structural Engineering* **130**(4), 618–630.

- Tran, T. A. and Wallace, J. W. [2012]. "Experimental study of nonlinear flexural and shear deformations of reinforced concrete structural walls," *Proc. of the 15th World Conf. on Earthquake Engineering*, Lisbon, Portugal.
- Vecchio, F. and Collins, M. P. [1981] "Stress-strain characteristics of reinforced concrete in pure shear," *Proc. of the IABSE Colloquium, Advanced Mech. of Reinforced Concrete IABSE Colloquium, Advanced Mechanics of Reinforced Concrete*, Delft, Final Report, Zurich, Switzerland, 221–225.
- Vecchio, F. J. and Collins, M. P. [1986] "The modified compression-field theory for reinforced concrete elements subjected to shear," *ACI Structural Journal* **83**(2), 219–231.
- Vulcano, A. and Bertero, V. V. [1987]. "Analytical models for predicting the lateral response of RC shear walls: evaluation of their reliability." EERC Rep. No. UCB/EERC-87/19, Earthquake Engineering Research Center, College of Engineering, University of California, Berkeley.
- Zhu, R. [2000] "Softened membrane model of cracked reinforced concrete considering the poisson effect," Ph.D. thesis, Dept. of Civil and Environmental Engineering, University of Houston, Houston, TX.